Research Article | Vol. 31, No. 19 / 11 Sep 2023 / Optics Express 31092
Optics EXPRESS

Demonstrating low Raman background in UV-written SiO_2 waveguides

MATHIAS NOVIK JENSEN,[1] JAMES C. GATES,[2] ALEX I. FLINT,[2] AND OLAV GAUTE HELLESØ[1,*]

[1]Department of Physics and Technology, UiT The Arctic University of Norway, Hansine Hansens veg 18, 9019 Tromsø, Norway
[2]Optoelectronics Research Centre, University of Southampton, University Road, SO17 1BJ Southampton, UK
[*]olav.gauge.helleso@uit.no

Abstract: Raman spectroscopy can give a chemical 'fingerprint' from both inorganic and organic samples, and has become a viable method of measuring the chemical composition of single biological particles. In parallel, integration of waveguides and microfluidics allows for the creation of miniaturized optical sensors in lab-on-a-chip devices. The prospect of combining integrated optics and Raman spectroscopy for Raman-on-chip offers new opportunities for optical sensing. A major limitation for this is the Raman background of the waveguide. This background is very low for optical fibers but remains a challenge for planar waveguides. In this work, we demonstrate that UV-written SiO_2 waveguides, designed to mimic the performance of optical fibers, offer a significantly lower background than competing waveguide materials such as Si_3N_4. The Raman scattering in the waveguides is measured in absolute units and compared to that of optical fibers and Si_3N_4 waveguides. A limited study of the sensitivity of the Raman scattering to changes in pump wavelength and in waveguide design is also conducted. It is revealed that UV-written SiO_2 waveguides offer a Raman background lower than −107.4 dB relative to a 785 nm pump and −106.5 dB relative to a 660 nm pump. Furthermore, the UV-written SiO_2 waveguide demonstrates a 15 dB lower Raman background than a Si_3N_4 waveguide and is only 8.7 – 10.3 dB higher than optical fibers. Comparison with a polystyrene bead (in free space, diameter 7 µm) reveal an achievable peak SNR of 10.4 dB, showing the potential of UV-SiO_2 as a platform for a Raman-on-chip device capable of measuring single particles.

1. Introduction

Waveguide enhanced Raman spectroscopy (WERS) offers long interaction lengths and strong interaction with an analyte by using the evanescent field of a high-index contrast waveguide. Coated nanophotonic silicon nitride waveguides have been used for detecting traces of chemical warfare agent stimulants down to 5 ppb [1]. Micromolar levels of cyclohexane have been probed in aqueous solutions with slot waveguides, again coated and made of silicon nitride [2]. This demonstrates the applicability to both gasses and liquids. The waveguides can be made by standard fabrication methods, are robust and can easily be integrated with microfluidics to make a lab-on-a-chip. Optical components like directional couplers, wavelength filters and grating input couplers can be fully integrated, and further integration or hybrid assembly with lasers and detectors is possible. As a first step towards integration, a packaged, fiber-coupled sensor has been demonstrated, with an integrated directional coupler for splitting the forward-propagating pump and the backward-propagating signal [3]. A recent and excellent review of WERS gives more details about the technique [4]. For biological applications, Raman spectroscopy offers label-free detection and chemical analysis. Currently, confocal Raman microscopy is gaining importance in the fields of biochemistry and microbiology [5–7] due to its ability to selectively sample cells and smaller volumes. For biological particles, the combination of Raman microscopy with optical

#498795 https://doi.org/10.1364/OE.498795
Journal © 2023 Received 23 Jun 2023; revised 18 Aug 2023; accepted 18 Aug 2023; published 6 Sep 2023

Optics EXPRESS

trapping can analyse particles down to the nanoscale [8]. The extension of WERS to applications in microbiology and for the analysis of biological nanoparticles may significantly increase the capabilities of lab-on-a-chip systems for these field. As a first step in this direction, the use of TriPleX waveguides has been proposed [9]. However, there are some significant hurdles to overcome. WERS is an alternative to surface enhanced Raman spectroscopy (SERS), which gives significantly higher Raman enhancement. A comparison of the two methods is beyond the scope of this article and we refer to the many good reviews of SERS, e.g. [10–12].

Among the limitations and challenges for waveguide enhanced Raman spectroscopy are propagation losses that limit the interaction length and the Raman background of the material. The Raman background induced from the waveguide material acts as a noise-signal that overlays the signal from the analyte/sample, thus the detection performance of a WERS device is fundamentally limited by the characteristics of the waveguide material. The application of waveguides for Raman spectroscopy can be divided into three general concepts:

- Evanescent field interaction: Interaction between the evanescent field and a homogeneous analyte along the waveguide length gives a large interaction volume and high sensitivity.
- Direct field interaction: Employing a slot or porous waveguide allows the analyte to intersect with the centre of the guided mode, again potentially giving high sensitivity for a homogeneous analyte.
- Field projection: To analyse a nanoparticle, high intensity at a point is necessary. This can be obtained with a hole in the waveguide, a trench across it or a structure that focus the mode onto the particle. Light is thus not guided, but projected onto the analyte for interaction in a small volume.

While both evanescent and direct field interactions give high coupling efficiencies and sensitivity, they are both most efficient for homogeneous analytes. Our work is focused on nanoparticles, for which field projection into a micron-sized volume is suitable. Thus, an embedded waveguide with negligible evanescent field interaction and high transmission is optimal. Optical fibers have extremely low propagation losses and it has been demonstrated that they also have a very low Raman background [13]. In this work, we investigate silica-based waveguides that are designed and fabricated to mimic the performance of silica fibers. The waveguides are made by UV-writing in doped silica, as will be described later. The waveguides have low refractive index contrast, a relatively large core, low propagation losses and low losses when end-coupling to an optical fiber [14–16]. However, as the waveguides are buried, with silica on all sides, there is no evanescent field available to do Raman spectroscopy of an analyte. Our approach will be to etch structures into the waveguide core (e.g. holes or trenches) for access to the field, for analysis of biological nanoparticles. Using a waveguide to project the trapping/exciting rather than using the evanescent field to excite Raman scattering enables the creation of a compact chip device with one or more micron-scale trapping sites suitable for nanoparticles.

In this article, we investigate the intrinsic properties of the waveguides for Raman scattering, without an etched interaction volume and without an analyte. The waveguides are measured using an in-line measurement scheme with a high-power laser acting as pump and a secondary, low power laser acting as a reference to obtain measurements on an absolute scale. The measurements are repeated for two pump wavelengths (660 nm and 785 nm) to evaluate the wavelength sensitivity of the background. This information will decide the choice of pump laser for future applications. Raman scattering increases with $1/\lambda^4$, possibly making a shorter wavelength favourable, but the background from the waveguide also depends on the wavelength. Thus, an experimental study is necessary to find which wavelength gives the best signal-to-noise ratio for a given waveguide and sample. The results are compared with Raman scattering in an optical fiber and in

Optics EXPRESS

a polystyrene bead (diameter 7 μm), with the first serving as a 'gold' standard and the second to estimate the achievable signal-to-noise ratio for an easily reproducible case. The results are also compared with a model and with published values. A limited study of the influence of waveguide dimensions, composition, and cladding material is included for the UV-written silica waveguides.

The Raman background of four common waveguide materials, Al_2O_3, Si_3N_4, Ta_2O_5, and TiO_2, has been compared previously [17], and its wavelength dependence for Si_3N_4 and Ta_2O_5 was studied by D. Coucheron et al. [18]. Only N. Le Thomas et al. [13] has previously reported absolute values for the Raman background (of Si_3N_4). Here, we report the absolute values for the Raman background of UV-written silica waveguides in comparison to previous measurements of Si_3N_4. Given the similarity between the silica waveguides and silica fibers in terms of mode size and composition, the absolute values for the Raman background of select fibers are also reported here.

The UV-written silica waveguides studied here have a low index contrast relative to those considered in previous works. The relative similarity between the investigated silica waveguides and silica fibers, which have been successfully implemented as Raman-probes, promotes such waveguides as an integrated optics platform for on-chip Raman spectroscopy.

Membrane waveguides has recently emerged as a new waveguide geometry [19], with a thin core surrounded by an analyte. The results presented here are also relevant for silica membrane waveguides, where the index contrast is between (undoped) silica and water. Thus, although the present results are for burried silica waveguides, several approaches can be envisioned to exploit the low Raman background measured by modifying the waveguide geometry locally or along the entire length, by making a membrane waveguide.

2. Model and expectations for Raman background in waveguides

Waveguide enhanced Raman spectroscopy requires the pump laser to propagate through a waveguide core made of a dense material with small cross-section, and it is thus expected that this propagation will generate substantial Raman scattering in the device itself. As a consequence, the Raman scattering collected from an analyte will also contain the Raman scattering from the waveguide as a background signal. This background represents the fundamental noise limit for Raman spectroscopy of the analyte, as stated in the introduction. The Raman spectrum of SiO_2 is readily available [20,21], but its intensity relative to the pump laser is necessary, for the waveguide considered, to compare it with the spectrum of an analyte. Before preceding to this measurement, a model for the background is useful for interpreting the results, although several of the parameters must be obtained by fitting to the measurements. N. Le Thomas *et al.* have proposed a model for the Raman scattering in optical waveguides [13]. The main equation of the model will be described and used here. The model aims to express the fundamental level of the Raman scattering in a dielectric waveguide by considering the stochastic fluctuations of the induced thermal field and the subsequent noise induced in the guided wave. In contrast to previous models based on standard diffusion [22,23], this model is derived from the concept of "frozen" thermal diffusion, where the decay time of a diffusion-driven heat flux is considered to be significantly longer than the decay of spontaneous heat fluxes induced in the medium. The shift in perspective from the "slow" diffusion to the much faster stochastic heat fluxes allows the effect of the fluctuations at higher frequencies, such as those relevant to Raman spectroscopy, to be considered. The fundamental level of frequency noise induced in a wave propagating through a medium can then be predicted using knowledge of the behaviour of the stochastic heat fluxes through their temporal and spatial correlation in the medium. The model is given by Eq. (10) in [13]:

$$I(\Omega) = {A_0}^2 \left\{ \delta(\Omega) + 4\pi^2 \left\langle \delta n^2 \right\rangle \frac{L\ell}{{\lambda_0}^2} \frac{\ell^2}{\ell^2 + 2W^2} \gamma e^{-\gamma|\Omega|} \right\}, \tag{1}$$

Optics EXPRESS

where A_0 denotes the initial field amplitude, $\delta(\Omega)$ the spectrum of the initial field, $\langle \delta n^2 \rangle$ the variance of the refractive index due to thermal fluctuations, L the length of the mode, λ_0 the excitation wavelength, and W the mode width. The additional variables ℓ and γ describe the spatial and temporal correlations of fluctuations in the temperature field, respectively.

As shown in Eq. (1), the inverse square dependence of the Raman intensity on the radial frequency shift Ω as seen in Eq. (35) in [23] is replaced by an exponential dependence due to the explicit consideration of temporal correlations in the thermal field. In the case of low frequency shifts Ω, the thermal fluctuations in the mode are assumed to be governed primarily by diffusion in the guiding medium. This results in an approximation of the Raman spectrum that is proportional to the inverse square of the frequency shift Ω. However, when Ω becomes large, the period of the propagating wave becomes much shorter than the correlation time of the diffusion, i.e. the inducing field oscillates faster than diffusion can propagate the generated heat. Using this assumption, the diffusion can be considered as a steady state phenomenon rather than reactive to the propagating wave. In this setting, both the temporal and spatial correlations of the thermal field can be considered as strong influences. Pursuing this assumption leads to an approximation of the Raman spectrum that is exponentially dependent on Ω when Ω is large. The influence of the temporal correlation is accounted for through the introduction of the characteristic time γ of the correlations. Similarly, the spatial correlations are accounted for through a characteristic length ℓ which has a linear dependence on γ (see Eq. (9) in [13]). Using these variables, along with the length L and width W of the guided mode, the thermal field δT can be modeled and connected to the optical field through the expected variance of the refractive index change $\langle \delta n^2 \rangle$. As we intend to filter out the pump wavelength ($\Omega = 0$), we see that the dirac-delta term $\delta(\Omega)$ becomes zero for all relevant Ω, allowing us to remove it from the expression. By also allowing the exciting field intensity A_0^2 to be an input variable, the model in Eq. (1) can be rewritten as:

$$I(\Omega)/I(0) = \left(4\pi^2 \frac{L}{{\lambda_0}^2}\right)\left(\langle \delta n^2 \rangle \frac{\ell^3}{\ell^2 + 2W^2}\gamma\right) e^{-\gamma|\Omega|}. \tag{2}$$

As the waveguide length L and pump wavelength λ_0 are known *a priori*, these can be collapsed into a known quantity $\alpha = 4\pi^2 L/\lambda_0^2$ for convenience. Of the four remaining variables, all but the mode width W are strongly dependent on the characteristics of the temperature field T and its fluctuations δT. Given the known dependencies on the material parameters listed in Table 1, it is possible to estimate these variables given the findings of N. Le Thomas [13]. However, as the exact characteristics of the thermal field fluctuations δT are not known, the variables dependent on it are collapsed into a fit parameter β. For convenience, the unknown characteristic time γ is replaced by a fit parameter ϵ such that the model can be expressed as a function of the wavenumber shift $\tilde{\nu}$ in cm^{-1} rather than the radial frequency shift Ω in rad/s. The model in Eq. (2) is thus rewritten as:

$$I(\tilde{\nu})/I(0) = \alpha\beta e^{-\epsilon\tilde{\nu}}, \tag{3}$$

with

$$\beta = \langle \delta n^2 \rangle \frac{\ell^3}{\ell^2 + 2W^2}\gamma \quad \text{and} \quad \epsilon = 2 \cdot 10^2 \pi c \gamma.$$

The model can then be fitted to the experimental results using the known parameter α and the fit parameters β and ϵ. Together with the model for Raman scattering in waveguides, N. Le Thomas *et al.* presented measurements of the Raman background in Si_3N_4-waveguides. The results showed a peak of −91.9 dB (normalised to 1 cm length, see Fig. 4 in [13]) with a decay given by a the characteristic time $\gamma = 13$ fs. Considering the material parameters of Si_3N_4 [13], as shown in Table 1, we see a number of differences between the parameters of Si_3N_4 and those of SiO_2. In the following, these differences will be described to find expectation values for the Raman background of UV-written silica waveguides.

Optics EXPRESS

Table 1. Material parameters for SiO_2 [25–29] and Si_3N_4 [13]: thermal conductivity κ_0, density ρ, heat capacity C_V, thermal expansion coefficient α_L, thermo-optic coefficient $\partial n/\partial T$, and refractive index n_ϕ. (*Mean values)

	$\kappa_0\left(\frac{W}{mK}\right)$	$\rho\left(\frac{g}{cm^3}\right)$	$C_V\left(\frac{J}{gK}\right)$	$\alpha_L\left(K^{-1}\right)$	$\frac{\partial n}{\partial T}\left(K^{-1}\right)$	n_ϕ
SiO_2	1.9	2.2*	0.73	$5.4{\cdot}10^{-7}$	$1.1{\cdot}10^{-5}$	1.5
Si_3N_4	25	2.5	0.17	$3.9{\cdot}10^{-6}$	$5{\cdot}10^{-5}$	1.8
Ratio	$9.3{\cdot}10^{-2}$	0.88	4.4	0.14	0.2	0.80

The thermal conductivity of SiO_2 is substantially lower than for Si_3N_4, which is expected to shorten the characteristic length ℓ of SiO_2 due to its square root dependence on thermal conductivity [13]. Factoring in the slightly lower density ρ and significantly higher heat capacity C_V we estimate the thermal diffusivity of SiO_2 to be 55 times weaker than for Si_3N_4, implying a correlation length ℓ that is 86.5% shorter for the same relaxation time τ. Considering that both the thermal expansion coefficient α and thermo-optic coefficient $\frac{\partial n}{\partial T}$ of SiO_2 is almost an order of magnitude smaller than for Si_3N_4 as well as the lower refractive index n_ϕ, it is implied that the variance of the refractive index $<\delta n^2>$ is approximately 96% smaller for SiO_2 than for Si_3N_4.

These material properties of SiO_2 compared to Si_3N_4 implies that the induced background of SiO_2 is significantly lower than for Si_3N_4. Factoring in the significantly larger mode field diameter of the UV-SiO_2 waveguides [15], it is implied that the Raman intensity of the UV-SiO_2 waveguide which is 18.3 dB weaker than for Si_3N_4, further implying a peak Raman intensity of -113.5 dB at $\tilde{\nu} = 530\text{cm}^{-1}$. This is in agreement with the measurements made by N. Le Thomas *et al.* on the PM-fiber (see Fig. S1 in [24]), as its peak corresponds to ≈ -114 dB when scaled to the same length.

As the materials of a PM-fiber and the silica waveguides are very similar, it is expected that the Raman spectrum of the waveguide will follow the same pattern as the PM-fiber as shown in Fig. S1 in the supplementary work of N. Le Thomas *et al.* [24]. However, given that the PM-fiber has a stated mode field diameter (MFD) of 5.3 μm while the UV-written waveguide has a MFD of approximately 5 μm, and since it is assumed that $\ell \ll W$, it is expected that the $\alpha\beta$-scalar for the waveguide is approximately 12% smaller than for the PM-fiber and its characteristic time $\approx$ 6% longer, assuming all other factors are equal. From this it is expected that the fiber and the waveguides will perform approximately the same, with the waveguide having a peak that is implied to be 1.1 dB lower than the fiber.

Regarding wavelength dependence, the equation derived by N. Le Thomas shows an inverse square dependence on the pump wavelength which implies a 1.5 dB stronger Raman background induced by a 660 nm pump compared to a 785 nm pump.

3. Experimental design

3.1. Waveguide fabrication

As depicted in Fig. 1, the fabrication begins by growing an oxide layer on a 150 mm diameter, 1 mm thick silicon wafer using a wet thermal process, common in microfabrication. On all the devices presented in this work, this layer is at least 15 μm thick and is high-purity silica. This layer will eventually serve as the bottom cladding of the waveguide, isolating the guided mode from the silicon underneath. Flame hydrolysis deposition (FHD) is then used to deposit a thick layer of doped silicate glass to serve as the core layer of the waveguide. The core is doped with germanium to provide UV photosensitivity, which is further enhanced by adding boron. Germanium and boron co-doping is conventionally used in UV-photosensitive optical fibers and planar waveguides. However, in this work, we have also investigated germanium and phosphorous co-doping. Lastly, an optional layer is added on top of the core to serve as a top

Optics EXPRESS

cladding to the waveguide. This layer is doped with phosphorus and boron to match the refractive index of the bottom silica-clad layer. The wafer is then diced into dies of approximately 10 x 20 mm and hydrogen loaded at 120 bar for several days to further enhance the UV photosensitivity [15,30]. The chip is then irradiated with two focused beams from a frequency-doubled argon-ion laser operating at a wavelength of 244 nm, see Fig. 1. UV exposure induces a localised increase in refractive index, thereby forming a channel waveguide.

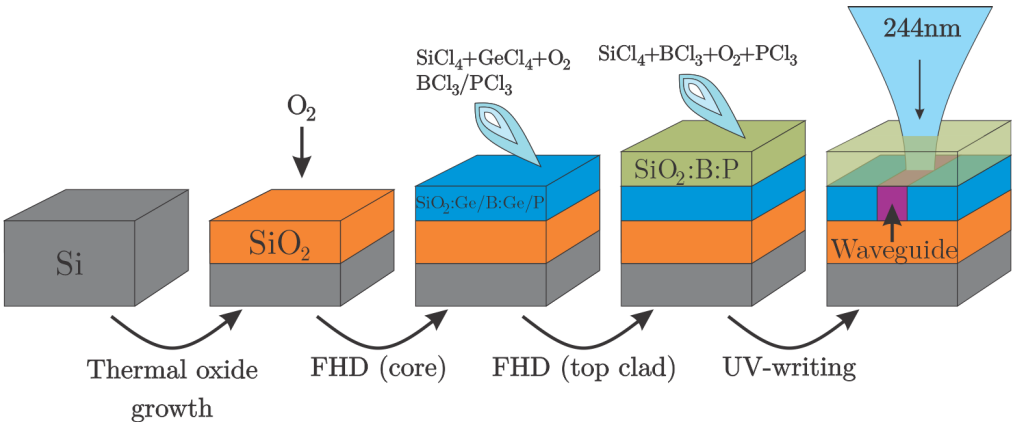

Fig. 1. Fabrication process for UV-SiO2 waveguides

Due to the weakness of the photorefractive effect, the Δn of the waveguide is low (typically $5 \cdot 10^{-3}$ [31]), resulting in a large mode and low NA, similar to standard optical fibers. The low Δn, along with the intrinsic smoothness of an etch-free waveguide, contribute to low propagation losses in the guided mode. The low loss, combined with the low NA ($\approx$ 0.1 [15]) allows these waveguides to project light with high power and low divergence into free space, but with lower intensity than a waveguide with high Δn. The low NA gives low loss across a gap in the waveguide, e.g. a hole or a trench, enabling several gaps in series for analysis of several samples along the waveguide. The large mode of these singlemode waveguides (MFD $\approx$ 5 µm) contributes to a low background in itself, as described in sec. 2.

3.2. Samples

Five waveguide chips are considered in this work to give a limited study of the sensitivity to waveguide design, all waveguides are of length $\approx$ 20 mm and are single mode for 660/785 nm wavelengths:

- Chip A: $\approx$ 5 µm **Ge+B** doped core layer with 17 µm B+P doped **top cladding**, MFD $\approx$ 5 µm @ 780 nm
- Chip B: $\approx$ 3 µm **Ge+B** doped core layer with $\approx$ 15 µm B+P doped **top cladding**, MFD $\approx$ 5 µm
- Chip C: $\approx$ 3 µm **Ge+P** doped core layer with **no top cladding**, MFD $\approx$ 5 µm
- Chip D_1 & D_2: $\approx$ 3 µm **Ge+B** doped core layer with **no top cladding**, MFD $\approx$ 5 µm

3.3. Experimental setup

The experimental setup, depicted in Fig. 2, consists of three main sections (a-c) and one auxiliary section (d).

Optics EXPRESS

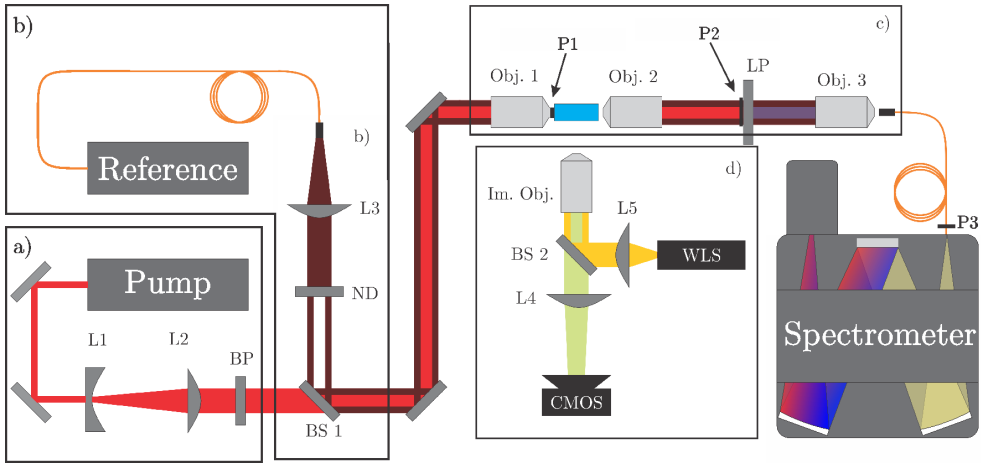

Fig. 2. Sketch of experimental setup for acquiring power Raman spectra of a sample waveguide. The path of the pump beam (red) moves through the entire setup untill removal by a long pass filter (LP) after out-coupling from the waveguide. A longer wavelength reference laser (brown) is joined to the pump path by a beam-splitte (BS 1) such that it bypasses the long pass filter and can be recorded by the spectrometer for calibration.

Section a

Section a is the origin of the pump beam, containing a high-power laser along with beam conditioning optics. To achieve best coupling to the waveguide, the output beam of the pump laser is expanded and collimated by a Galilean beam expander (L1 and L2) such that it yields a plane wave field with gaussian profile and width that is compatible with the back aperture of the in-coupling objective. The beam is also passed through a narrow band-pass filter (BP) such that the side-bands of the laser are suppressed, with special attention to the longer wavelengths.

Section b

Section b is the origin of the reference beam, accepting a fiber coupled laser source of wavelength longer than the pump beam and merging it to a common path with the pump beam. The fiber output is collimated by an appropriate lens (L3) such that it yields a gaussian plane wave that is coupled to a common path with the pump beam by a 90:10 beam splitter (BS 1).

Section c

Section c is the central part of the setup, containing the waveguide as well as the in-coupling (obj. 1) and out-coupling (obj.2) objectives. The output of the waveguide is, after collimation by the out-coupling objective, passed through a long-pass filter (LP) that removes the transmitted pump beam, leaving the Raman scattering and the reference beam. The filtered output is then coupled to a fiber by a final objective (obj. 3) and passed to the spectrometer.

Section d

Section d is a microscope for imaging the surface of the chip and for assisting in coupling to and from the waveguide, thus is an auxiliary section of the setup and does not contribute to the Raman measurements. This tower consists of a white light source (WLS) focused on the back focal plane of the imaging objective (Im. Obj.) by a lens (L5) relayed via a pellicle beam splitter (BS 2). Images are obtained by focusing the backscatter by a tube lens (L4) onto a camera (CMOS) for acquisition.

Optics EXPRESS

Components

- Pump: 660 nm DPSS (HüBNER, Cobolt 05-01) or 785 nm DPSS (CrystaLaser, DL785-100)
- Reference: 686 nm diode laser (ThorLabs, LP685-SF15) or 826 nm diode laser (ThorLabs, LPS-830-FC)
- Spectrometer: Multi-grating spectrometer (300/g, 600/g & 1200/g), focal length 320 mm (Teledyne Princeton, IsoPlane SCT320) with deep depletion CCD (Teledyne Princeton, BLAZE 400BR)
- Obj. 1: 10x objective (Olympus PLN10X, 10x 0.25NA) mounted on three axis stage with closed loop piezo (ThorLabs, MAX331D/M)
- Obj. 2: 10x objective (Olympus PLN10X, 10x 0.25NA) mounted on three axis stage (ThorLabs, MAX313D/M)
- Obj. 3: 10x objective (Olympus PLN10X, 10x 0.25NA) mounted on three axis stage (ThorLabs, 313D/M)
- BP: 660 ± 13 nm band-pass for 660 nm pump (Semrock, BrightLine FF01-660/13-25), 785 ± 3 nm for 785 nm pump (Edmund optics, 64-257)
- LP: 664 nm ultrasteep long-pass for 660 nm pump (Semrock, RazorEdge LP02-664RU-25) or 785 nm ultrasteep long-pass for 785 nm (Semrock, RazorEdge LP92-785RE-25)

3.4. Power calibration

Determining the spectrum of the Raman scattering induced in the waveguide is a relatively trivial task, requiring only subtraction of the background and correcting for the spectral sensitivity of the setup. However, in order to compare different waveguides and infer the intensity of the background in a Raman-on-chip device built from those waveguides requires a more thorough calibration such that the spectra can be expressed in absolute intensity rather than arbitrary units. This is why the reference laser (see Fig. 2) is necessary, providing a power reference that bypasses the long-pass filter such that it can be used as an intermediate bridge to compare the Raman spectra with the pump intensity. This requires a set of common measurement points (P1 and P2 in Fig. 2) where the pump and reference beams can be compared and a common point where the reference beam and the Raman scattering can be compared (P3 in Fig. 2). The goal of this is to obtain a calibration spectrum $C(\tilde{\nu})$ such that the intensity spectrum $I(\tilde{\nu})$ can be expressed from the measured spectrum $S(\tilde{\nu})$ as:

$$I(\tilde{\nu}) = C(\tilde{\nu})\, S(\tilde{\nu})\, (mW). \tag{4}$$

In order to express the measured spectrum as a calibrated spectrum, the measured spectrum must first be corrected for spectral background and sensitivity. As the background spectrum $S_{BG}(\tilde{\nu})$ introduces a constant bias to the measured spectrum $S'(\tilde{\nu})$, this must first be subtracted. The spectral sensitivity $A(\tilde{\nu})$ of the setup must also be accounted for such that the spectrum is not distorted. This is done by measuring a known source (Teledyne Princeton Halogen calibration lamp) and determining the relative response of the setup. The spectral sensitivity $A(\tilde{\nu})$ is then determined from the curve such that it scales to 1 at the reference laser wavelength

Optics EXPRESS

$(A\left(\lambda = \lambda_{Ref}\right) = 1)$. The true spectrum can then be approximated by the unbiased and distortion-free estimate spectrum:

$$\hat{S}\left(\tilde{\nu}\right) = A^{-1}\left(\tilde{\nu}\right)\left[S'\left(\tilde{\nu}\right) - S_{BG}\left(\tilde{\nu}\right)\right], \tag{5}$$

allowing Eq. (4) to be expressed as:

$$I\left(\tilde{\nu}\right) = c_1 A^{-1}\left(\tilde{\nu}\right) \cdot \left(S'\left(\tilde{\nu}\right) - S_{BG}\left(\tilde{\nu}\right)\right), \tag{6}$$

where $C\left(\tilde{\nu}\right)$ is replaced by $c_1 A^{-1}\left(\tilde{\nu}\right)$.

With the spectral elements of $C\left(\tilde{\nu}\right)$ being separated into the sensitivity curve $A^{-1}\left(\tilde{\nu}\right)$, the remaining calibration coefficient c_1 can be obtained by measuring the intensity of the pump and reference laser at in-coupling to the waveguide (P1 in Fig. 2) and at the fiber output (P3 in Fig. 2). This is done by first determining the scaling between mW and CCD counts through the coefficient c_0 using the measured intensity of the reference laser at the spectrometer (P3 in Fig. 2) $P3_{Ref}$ and a measured spectrum of the reference laser $S_{Ref}\left(\tilde{\nu}\right)$ along with the known attenuation factor A_{ND} of the neutral density filter (ND in Fig. 2). The coefficient c_0 can thus be expressed as:

$$c_0 = \frac{P3_{Ref}}{A_{ND}\sum_{n=0]}^{N}\hat{S}\left[\tilde{\nu}_n\right]},$$

where $\hat{S}\left[\tilde{\nu}_n\right]$ is the discrete spectrum of the reference laser source.

Finally, since the setup will have a difference in coupling and propagation losses for the pump and reference beams, this must also be taken into account. Using measurement points P1 and P3, the pump transmission can be expressed as:

$$T_{pump} = \frac{P3_{pump}}{P1_{pump}},$$

and the reference transmission as:

$$T_{Ref} = \frac{P3_{Ref}}{P1_{Ref}},$$

such that the calibration coefficient c_1 can be expressed as:

$$c_1 = c_0 \cdot \frac{T_{Ref}}{T_{Pump}}. \tag{7}$$

We can then substitute Eq. (7) into Eq. (6) to express the calibrated spectrum in Eq. (4) using measurable factors:

$$I\left(\tilde{\nu}\right) = \frac{T_{Ref}}{T_{Pump}}\frac{P3_{Ref}}{P1_{Pump}A_{ND}\sum_{n=0]}^{N}\hat{S}\left[\tilde{\nu}_n\right]} \cdot A^{-1}\left(\tilde{\nu}\right)\left(\hat{S}\left(\tilde{\nu}\right) - S_{BG}\left(\tilde{\nu}\right)\right). \tag{8}$$

3.5. Composite spectra

To fully take advantage of the spectrometer's capabilities and the fact that the fiber-coupled input (ThorLabs, SM-830) gives an effective slit width of approx. 5 µm, we choose to use the finest grating available (1200g/mm) to achieve a dispersion of 2.30 nm/mm at the focal plane. With a CCD pixel size of 20 µm, this yields a per pixel resolution of 0.05 nm but limits the spectral range of each acquisition to 52.3 nm. Therefore, the entire range of the Raman scattering (240 – 365 nm) cannot be captured in a single acquisition without compromising resolution. A one-shot acquisition also demands the dynamic range of the spectrum is within the dynamic range of the CCD (48.2 dB) and above the noise floor. Given the expected exponential decay of the signal with increasing wavenumber shift, as discussed in Sec. 2 a uniform spectral sensitivity risks

Optics EXPRESS

either over-saturating the CCD at low wavenumber shift, where the signal is strong, or losing the signal to noise at high wavenumber shift, where the signal is weak.

To solve this, we propose dividing the spectral range into segments that can be individually measured and later be merged in post-processing to obtain a composite spectrum covering an arbitrary spectral range. This allows us to acquire the entire spectral range without sacrificing the resolution afforded by the fine grating. This also allows us to dynamically select the exposure time and number of repeat exposures for each segment separately such that the SNR and dynamic range usage can be normalized for each segment separately.

This method is implemented through an automated script (Python 3.8.10) that partitions the desired range into a set of overlapping segments, each with their own exposure time t_e and number of averaged acquisitions n_{avg}. The acquisition parameters t_e and n_{avg} are then estimated using an initial guess for the exponential decay of the spectra such that the expected signal fills $\approx 10\%$ of the dynamic range of the CCD. A test acquisition of three spectra per segment is then made such that the parameters SNR and dynamic range usage can be estimated. This is achieved by a rough separation of the signal and CCD noise by low-pass filtering the measurement, using the low-frequency elements as a signal estimator and the high-frequency elements as a noise estimator. The signal estimator is then used to tune the dynamic range usage through the exposure time t_e while the noise estimator is used to tune the SNR to an acceptable level ($\geq$ 10dB) through increasing the number of averaged spectra n_{avg} in that segment. Using the determined parameters, the spectra of each segment is acquired and cleaned for background and cosmic rays. Using a least squares fit of their overlap, the segments are adjusted for their varying sensitivity and level of dark signal such that they are brought to a uniform scale with the first segment and can then be merged to form the composite spectrum.

4. Results

4.1. Pump wavelength: 600 nm vs. 785 nm

As previously mentioned in Sec. 1, one of the objectives of this work is to evaluate the sensitivity of the Raman scattering of the UV-SiO_2 waveguides to the wavelength of the pump lasers. To this end, the experiment is repeated with two sets of pump and reference lasers, first using a 660 nm pump complemented by a 686 nm reference and then using a 785 nm pump complemented by a 826 nm reference. These two pump wavelengths were chosen because of the availability of high-power lasers with high spectral purity and that both wavelengths are commonly used in Raman spectroscopy.

As described by N. Le Thomas *et al.* [13] and shown in the α component in Eq. (3), the intensity of the Raman scattering in the guided mode is expected to have an inverse square dependence on the pump wavelength λ_0. From this, it is expected that using $\lambda_0 = 660$ nm will induce Raman scattering approximately 1.5 dB stronger than using $\lambda_0 = 785$ nm, indicating that 785 nm may be favourable for a Raman-on-chip device. The use of 785 nm may also help reduce undesirable fluorescence in the waveguide and/or analyte compared to 660 nm, thus separating the Raman spectrum from the flourescence spectrum. However, the signal from a particle intersecting the beam path is expected to be proportional to λ^{-4}, implying a 3 dB increase in signal when using 660 nm instead of 785 nm as the pump wavelength, potentially compensating for the increased background in the waveguide. Another benefit of using a 660 nm pump is that it allows a longer range of wavenumber shift to be measured using a high-quality silicon-based CCD.

This enables us to acquire measurements up to 5 400cm^{-1} without exceeding the useful range of the spectrometer camera ($\lambda \leq 1025$ nm) while using 785 nm only allows for measurements up to 3 000 cm^{-1}. A pump of 660 nm thus allows for measurement of features in a wavenumber range where the background from the waveguide is expected to be negligible. One significant challenge with using shorter pump wavelength is the increased potential to induce fluorescence,

Optics EXPRESS

both from the analyte and the waveguide material, which would mask the Raman signal. The measurements are obtained from two waveguide chips, chip A for 785 nm and chip B for 660 nm. For reference, the same fiber as used by N. Le Thomas *et al.* [24] is measured with both pump wavelengths, as is a 7 μm polystyrene bead to demonstrate the achievable SNR compared to a particle. As shown in Fig. 3, both the waveguides and the PM-fiber exhibit stronger Raman scattering when excited with 660 nm, notably so with the appearance of a flattening of the spectra as the shift exceeds ≈ 1500 cm^{-1}. Given that this flattening forms a wide bulge and is only present when excited with 660 nm, this is more consistent with fluorescence than Raman. Aside from this, we can see that the levels and features of the two pairs remain almost identical prior to the flattening and that the features of the PS-bead are almost identical.

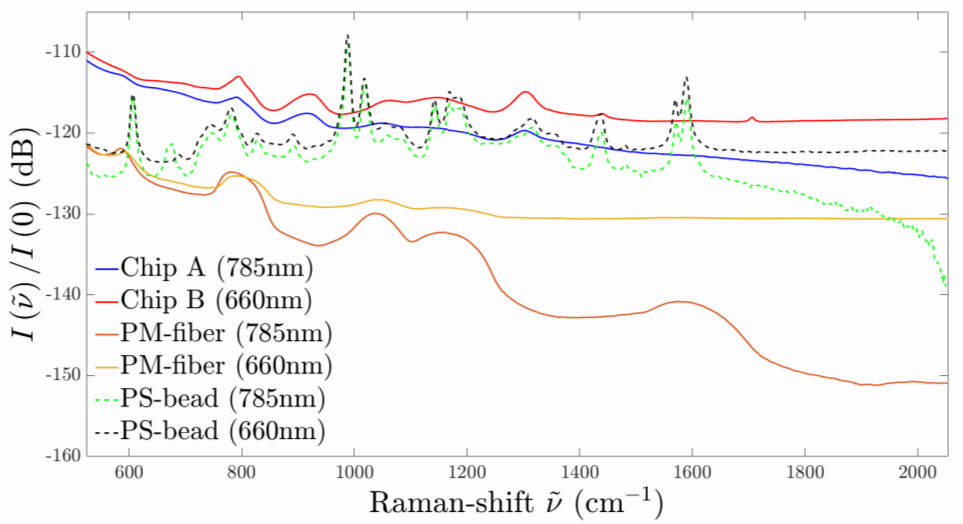

Fig. 3. Raman background spectra for waveguide chips A and B (with top cladding) compared to a PM-fiber with a single 7 μm polystyrene bead for reference, measured for two separate pump wavelengths (660 nm and 785 nm).

In terms of features, we see that both waveguides exhibit a peak at ≈ 920 cm^{-1} that is absent in the spectrum of the fiber, this can be readily assigned to the stretching mode of Ge-O-Si [32] due to the known high concentration of germanium in the waveguide cores. We can also observe that both waveguides produce peaks at ≈ 1310 cm^{-1} that corresponds well with B-O^- [33] as is also expected due to the boron-doping of the core. The remaining features at ≈ 1440 cm^{-1} and ≈ 1710 cm^{-1} may also be due to B-O-B and $[BO_3]^+$ modes, but due to the ambiguity of features near those shifts, we are hesitant to make the assignment. One other noteworthy observation in the Raman spectra is the significantly weaker feature at ≈ 580 cm^{-1} in the waveguides compared to the fiber. This is commonly assigned as a defect mode of Si-O-Si [34], which diminishes with increasing dopant concentration as observed here.

Because of the higher background produced by the waveguide when excited using 660 nm compared to 785 nm and the fact that the PS-bead, serving as an analogue for future particles, shows only a weak increase in feature intensity when excited using 660 nm, it is concluded that 785 nm is the preferred pump wavelength for this type of waveguide device.

4.2. Dependence on doping and cladding

Another objective is to determine the sensitivity of the Raman scattering on the doping of the core layer and the use of a top cladding. In this section, three additional chips (C,D_1 and D_2) are

Optics EXPRESS

measured using a 785 nm pump. For reference, both the fully clad NIR-waveguide (chip A) and the PM-fiber shown in Fig. 3 are included. As mentioned in Sec.3.2, both chips C and D are manufactured without top cladding while chips A and B are manufactured with a top cladding (>10 μm B+P doped SiO_2). Chip C is doped with phosphorous instead of boron while chips D are doped similarly to chips A and B. As shown in Fig. 4, the results from chip A and chips D_1 and D_2 match well, as expected, and it can be seen that the measurements obtained from two waveguides from D_1 and two from D_2 group well, supporting consistency of the power calibration. We also see that the phosphorous doped chip C performs significantly poorer than the other chips, producing a noticeably flatter Raman spectrum with a higher baseline than the other samples. The measured transmission through chip C was up to 5.6dB lower than either chip D and the mode at the output was poorly defined with significant slab guiding in the core layer relative to the guiding in the UV-written waveguide. The high degree of slab guiding indicates poor lateral confinement, likely due a low Δn being induced by the photorefractive effect without the presence of boron doping. Several of the chips, notably chip D_1, also displayed a significant variance in transmission between waveguides, varying as much as 5.4dB. The variance in transmission among the topless waveguides suggests chipping or defects at the facet because of a lack of the protective top cladding. The low and varying transmission for some of the waveguides may thus be due to poor in-coupling and surface defects, rather than absorption or scattering in the core itself.

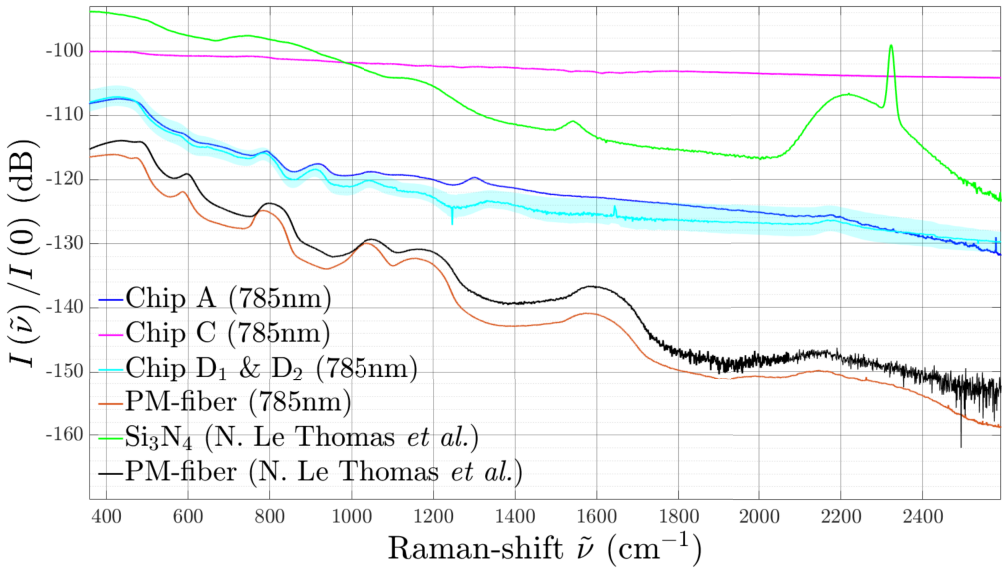

Fig. 4. Measurement of all chips with PM-fiber for comparison. Previously reported measurements of Si_3N_4 and similar PM-fiber are also included for reference.

4.3. *Fitting the spectra to the model*

In this section, the measured spectra are fitted to the model described in eq. (3) and the parameters of the fit are compared between the measured waveguides and previously reported measurements. The fits are shown in Fig. 5. The general level of the measurements follow the model in Eq. (3) well, with the majority of deviance being due to specific features in the Raman spectra. We also see from the parameters and peak intensity in Table 2 that our measurements of the PM-fiber agree with those made by N. Le Thomas *et al.* [24] in both profile and intensity. From the listed intensities we see that all of the Ge+B-doped SiO_2 (Chips A, B, D_1 and D_2) have a negligible

Optics EXPRESS

difference in peak amplitude, while the P+Ge-doped SiO_2 (Chip C) has a peak 6 dB higher than the rest, emphasizing the negative effect of phosphorous in the core. Lastly, we see that the Raman scattering in our UV-SiO_2 waveguides is more than 12 dB weaker than what is reported for Si_3N_4, reinforcing their advantage for Raman-applications.

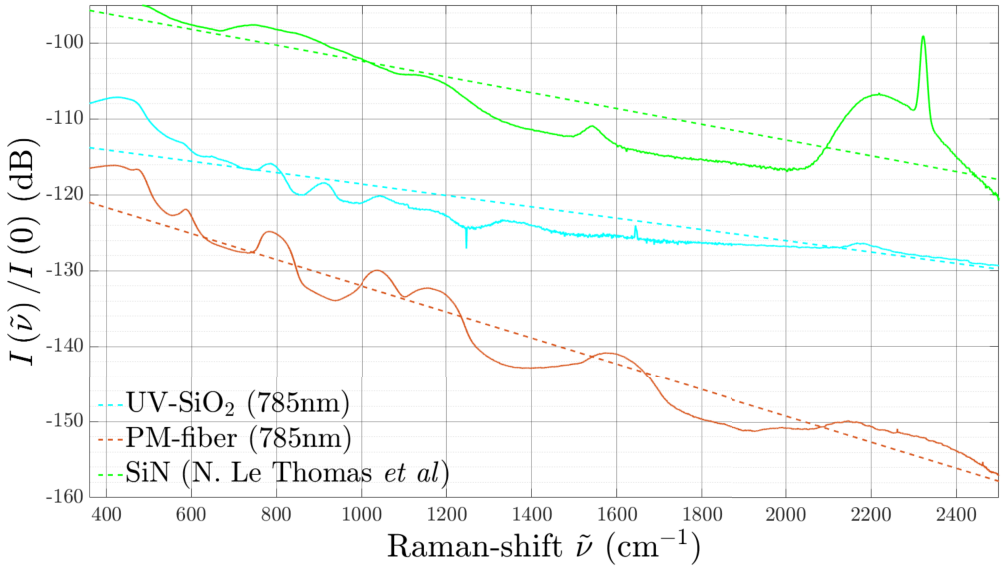

Fig. 5. Fit of the model in eq. (3) to measurements of chips A, B, C, D_1 and D_2 with a similar PM-fiber measured in this work and in the work of N. Le Thomas *et al.* as a reference. The fit of reported measurements of a Si_3N_4 waveguide is also added for comparison with the UV-written SiO_2 waveguides.

Table 2. Table of fit parameters for spectra in Fig. 5 to Eq. (3) as described in Sec. 2. *All measurements are scaled to emulate a length of 1cm

Sample\Parameter	α^* $\left(m^{-1}\right)$	β (ms)	ϵ (m)	I_{max} (dB)	RMSe (dB)
Chip A	6.4e">+27	2.3e-32	2.2e-5	−107	2.2
Chip B (660nm)	9.1e">+27	5.2e-33	5.7e-6	−106	3.8
Chip C	6.4e">+27	5.8e-32	3.7e-6	−100	0.3
Chip D	6.4e">+27	1.5e-32	1.9e-5	−107	2.4
PM780-fiber	6.4e">+27	5.2e-33	4.0e-5	−116	2.6
PM780-fiber [24]	6.4e">+27	1.0e-32	4.1e-5	−114	2.9
Si_3N_4 [13]	6.4e">+27	1.0e-30	2.4e-5	−94	4.3

5. Conclusion

The Raman background of UV-written silica waveguides has been measured and compared to other platforms, notably Si_3N_4 waveguides and (silica) optical fibers. To obtain results in absolute terms, the acquired spectra were calibrated to the input intensity. This was achieved using a separate laser source, acting as a reference and coupled into a common path with the pump laser, such that both the Raman spectra and the reference laser could be measured with the same configuration. Furthermore, by combining the spectrum of a reference source measured by

Optics EXPRESS

a spectrometer with the power of the pump and reference source measured by a photodiode power meter, the acquired Raman spectra were calibrated to absolute terms. To take full advantage of the setup, a high-resolution grating (1200 lines/mm) is used and the spectra are acquired in adjoining segments, allowing the full spectral and dynamic range of the spectrometer to be used. The acquisition time and number of repetitions was set independently for each section, to exploit the full range of the CCD spectrometer and to tailor the sensitivity to the expected intensity for the section. This allowed a high signal-to-noise ration for a very large dynamic range (from −100 to −160 dB relative to the pump laser).

The background of the UV-written SiO_2 waveguides was measured for two excitation wavelengths, 660 nm and 785 nm. Waveguides written into five chips were characterized, and for reference two optical fibers and a 7 μm polystyrene bead were also measured. This revealed a Raman intensity of less than −107.4 dB in the biochemical fingerprint region for a waveguide excited by 785 nm, and less than −106.5 dB when excited by 660 nm (normalised to 1 cm length). The difference increased for increasing wavenumber shifts, leading to the conclusion that 785 nm is better suited than 660 nm when using these waveguides. This conclusion depends on signal-to-noise ratio, which depends on the analyte, and it was shown that it holds for a polystyrene bead as it gave the same Raman signal for both wavelengths. The largest peak in the Raman spectrum of a 7 μm PS-bead was 10.4 dB higher than the waveguide background. This shows that a good signal-to-noise ratio can be obtained for microparticles with all the background from a 1 cm long waveguide collected as noise. The signal scales with the intensity and the interaction volume, with the first depending on the waveguide structure for illuminating the particle (e.g. hole, trench or taper) and the second on the diameter of the particle. The noise depends on how much of the waveguide background is collected (e.g. by a microscope objective or a collection waveguide). The achievable signal-to-noise ratio for nanoparticles thus depends on the interaction structure and the collection method. We will investigate this in future work.

The background induced in the best waveguide was 8.7 − 10.3 dB higher than for optical fibers and approximately 15 dB smaller than for Si_3N_4 waveguides [13]. UV-written waveguides thus present a very promising alternative for on-chip Raman spectroscopy, but there is still room for improvement when comparing with optical fibers.

A limited study of the impact of doping was made, with phosphorous doping giving significantly higher background than boron, with −100.0 dB and −106.5 dB, respectively, for a wavenumber shift of 410 cm^{-1} and 436 cm^{-1}. In addition, the phosphorous doping resulted in a significant flattening of the spectrum and poor waveguide confinement. This may have influenced the result. The presence or not of a top-cladding did not influence the background significantly (for boron doped samples). The background of four top-clad waveguides from two chips deviated by less than 5.7 dB over the entire fingerprint region, showing good repeatability considering the mean level of −121 dB.

This work has only considered the noise related to Raman background of the waveguides, and the logical next step will be to modify the waveguides to obtain signals from an analyte. Several procedures will be tested, notably etching trenches across the waveguides. Approaches for incorporating more complex structures, such as tapers and/or nanoantennas will also be explored.

Funding. The publication charges for this article have been funded by a grant from the publication fund of UiT The Arctic University of Norway. Norges Forskningsråd (302333).

Acknowledgments. The authors thank Dr. Cees Otto for useful discussions and suggestions. The authors would also like to thank Dr. Nicolas Le Thomas for providing the original data from his work [13,24] on Si_3N_4 waveguides and a SiO_2 PM-fiber.

Disclosures. The authors declare no conflic of interest.

Data availability. Acquired data is available in open source database (Dataverse UiT, DOI:10.18710/R6JHV7). The spectra of PM-fibers acquired by N. Le Thomas *et al.* and displayed in Figs. 4 and 5 are detailed in Ref. [13] and [24].

Optics EXPRESS

References

1. N. F. Tyndall, T. H. Stievater, D. A. Kozak, K. Koo, R. A. McGill, M. W. Pruessner, W. S. Rabinovich, and S. A. Holmstrom, "Waveguide-enhanced raman spectroscopy of trace chemical warfare agent simulants," Opt. Lett. **43**(19), 4803–4806 (2018).
2. N. L. Thomas, Z. Liu, C. Lin, H. Zhao, and R. Baets, "Raman on-chip: current status and future tracks," in *Integrated Optics: Devices, Materials, and Technologies XXV*, vol. 11689 S. M. García-Blanco and P. Cheben, eds., International Society for Optics and Photonics (SPIE, 2021), p. 1168908.
3. D. M. Kita, J. Michon, and J. Hu, "A packaged, fiber-coupled waveguide-enhanced raman spectroscopic sensor," Opt. Express **28**(10), 14963–14972 (2020).
4. M. A. Ettabib, A. Marti, Z. Liu, B. M. Bowden, M. N. Zervas, P. N. Bartlett, and J. S. Wilkinson, "Waveguide enhanced raman spectroscopy for biosensing: A review," ACS Sens. **6**(6), 2025–2045 (2021).
5. H. Jayan, H. Pu, and D.-W. Sun, "Recent developments in raman spectral analysis of microbial single cells: Techniques and applications," Crit. Rev. Food Sci. Nutr. **62**(16), 4294–4308 (2022). PMID: 34251940.
6. G. Pezzotti, "Raman spectroscopy in cell biology and microbiology," J. Raman Spectrosc. **52**(12), 2348–2443 (2021).
7. E. S. L. J. Hong, S. B. Kim, and T. K. Lee, "Microbial phenomics linking the phenotype to function: The potential of raman spectroscopy," J. Microbiol. **59**(3), 249–258 (2021).
8. W. Lee, A. Nanou, L. Rikkert, F. A. W. Coumans, C. Otto, L. W. M. M. Terstappen, and H. L. Offerhaus, "Label-free prostate cancer detection by characterization of extracellular vesicles using raman spectroscopy," Anal. Chem. **90**(19), 11290–11296 (2018). PMID: 30157378.
9. M. Boerkamp, T. van Leest, J. Heldens, A. Leinse, M. Hoekman, R. Heideman, and J. Caro, "On-chip optical trapping and raman spectroscopy using a triplex dual-waveguide trap," Opt. Express **22**(25), 30528–30537 (2014).
10. J. Langer, D. J. de Aberasturi, and J. Aizpurua, *et al.*, "Present and future of surface-enhanced raman scattering," ACS Nano **14**(1), 28–117 (2020).
11. M. Fan, G. F. S. Andrade, and A. G. Brolo, "A review on recent advances in the applications of surface-enhanced raman scattering in analytical chemistry," Anal. Chim. Acta **1097**, 1–29 (2020).
12. C. Zong, M. Xu, L.-J. Xu, T. Wei, X. Ma, X.-S. Zheng, R. Hu, and B. Ren, "Surface-enhanced raman spectroscopy for bioanalysis: Reliability and challenges," Chem. Rev. **118**(10), 4946–4980 (2018).
13. N. Le Thomas, A. Dhakal, A. Raza, F. Peyskens, and R. Baets, "Impact of fundamental thermodynamic fluctuations on light propagating in photonic waveguides made of amorphous materials," Optica **5**(4), 328–336 (2018).
14. Q. S. Ahmed, P. C. Gow, C. Holmes, P. L. Mennea, J. W. Field, R. H. Bannerman, D. H. Smith, C. B. Gawith, P. G. Smith, and J. C. Gates, "Direct uv written waveguides and bragg gratings in doped planar silica using a 213 nm laser," Electron. Lett. **57**(8), 331–333 (2021).
15. G. Lepert, M. Trupke, E. A. Hinds, H. Rogers, J. C. Gates, and P. G. R. Smith, "Demonstration of uv-written waveguides, bragg gratings and cavities at 780 nm, and an original experimental measurement of group delay," Opt. Express **19**(25), 24933–24943 (2011).
16. P. C. Gow, R. H. S. Bannerman, P. L. Mennea, C. Holmes, J. C. Gates, and P. G. R. Smith, "Direct uv written integrated planar waveguides using a 213 nm laser," Opt. Express **27**(20), 29133–29138 (2019).
17. A. Raza, S. Clemmen, P. Wuytens, M. de Goede, A. S. K. Tong, N. Le Thomas, C. Liu, J. Suntivich, A. G. Skirtach, S. M. Garcia-Blanco, D. J. Blumenthal, J. S. Wilkinson, and R. Baets, "High index contrast photonic platforms for on-chip raman spectroscopy," Opt. Express **27**(16), 23067–23079 (2019).
18. D. A. Coucheron, Ø. I. Helle, J. S. Wilkinson, G. S. Murugan, C. Domínguez, H. Angelskår, and B. S. Ahluwalia, "Study of waveguide background at visible wavelengths for on-chip nanoscopy," Opt. Express **29**(13), 20735–20746 (2021).
19. M. Vlk, A. Datta, S. Alberti, A. Aksnes, G. S. Murugan, and J. Jagerska, "High-aspect-ratio free-standing membrane waveguides for mid-infrared nanophotonics," in *2021 Conference on Lasers and Electr-optics (CLEO)*, (IEEE, 2021), Conference on Lasers and Electro-Optics. Conference on Lasers and Electro-Optics (CLEO), ELECTR NETWORK, MAY 09-14, 2021.
20. D. Giordano, D. González-García, J. K. Russell, S. Raneri, D. Bersani, L. Fornasini, D. Di Genova, S. Ferrando, M. Kaliwoda, P. P. Lottici, M. Smit, and D. B. Dingwell, "A calibrated database of raman spectra for natural silicate glasses: implications for modelling melt physical properties," J. Raman Spectrosc. **51**(9), 1822–1838 (2020).
21. T. Geisler, L. Dohmen, C. Lenting, and M. B. K. Fritzsche, "Real-time in situ observations of reaction and transport phenomena during silicate glass corrosion by fluid-cell raman spectroscopy," Nat. Mater. **18**(4), 342–348 (2019).
22. S. Foster, "Low-frequency thermal noise in optical fiber cavities," Phys. Rev. A **86**(4), 043801 (2012).
23. S. Foster, A. Tikhomirov, and M. Milnes, "Fundamental thermal noise in distributed feedback fiber lasers," IEEE J. Quantum Electron. **43**(5), 378–384 (2007).
24. N. L. Thomas, A. Dhakal, A. Raza, F. Peyskens, and R. G. Baets, "Supplement 1.pdf," (2018).
25. J. M. Larkin and A. J. H. McGaughey, "Thermal conductivity accumulation in amorphous silica and amorphous silicon," Phys. Rev. B **89**(14), 144303 (2014).
26. S. Inaba, S. Oda, and K. Morinaga, "Heat capacity of oxide glasses measured by ac calorimetry," J. Non-Cryst. Solids **306**(1), 42–49 (2002).
27. H. Gao, Y. Jiang, Y. Cui, L. Zhang, J. Jia, and L. Jiang, "Investigation on the thermo-optic coefficient of silica fiber within a wide temperature range," J. Lightwave Technol. **36**(24), 5881–5886 (2018).

Optics EXPRESS

28. G. Pan, N. Yu, B. Meehan, T. W. Hawkins, J. Ballato, and P. D. Dragic, "Thermo-optic coefficient of b_2o_3 and geo_2 co-doped silica fibers," Opt. Mater. Express **10**(7), 1509–1521 (2020).
29. H. J. Lee, F. Abdullah, S. D. Emami, and A. Ismail, "Fiber modeling and simulation of effective refractive index for tapered fiber with finite element method," in *2016 IEEE 6th International Conference on Photonics (ICP)*, (2016), pp. 1–3.
30. H. L. Rogers, C. Holmes, J. C. Gates, and P. G. R. Smith, "Analysis of dispersion characteristics of planar waveguides via multi-order interrogation of integrated bragg gratings," IEEE Photonics J. **4**(2), 310–316 (2012).
31. R. M. Parker, J. C. Gates, M. C. Grossel, and P. G. Smith, "A temperature-insensitive bragg grating sensor—using orthogonal polarisation modes for in situ temperature compensation," Sens. Actuators, B **145**(1), 428–432 (2010).
32. J. Zhao, Z. Yang, C. Yu, J. Qiu, and Z. Song, "Influence of glass composition on photoluminescence from ge^{2+} or ag nano-cluster in germanate glasses for white light-emitting diodes," J. Am. Ceram. Soc. **102**(3), 1169–1179 (2019).
33. A. K. Yadav and P. Singh, "A review of the structures of oxide glasses by raman spectroscopy," RSC Adv. **5**(83), 67583–67609 (2015).
34. K. Sasan, A. Lange, T. D. Yee, N. Dudukovic, D. T. Nguyen, M. A. Johnson, O. D. Herrera, J. H. Yoo, A. M. Sawvel, M. E. Ellis, C. M. Mah, R. Ryerson, L. L. Wong, T. Suratwala, J. F. Destino, and R. Dylla-Spears, "Additive manufacturing of optical quality germania-silica glasses," ACS Appl. Mater. Interfaces **12**(5), 6736–6741 (2020).